PR12-13-009

(A proposal to Jefferson Lab PAC40)

Wide-angle Compton Scattering at 8 and 10 GeV Photon Energies

D. J. Hamilton (co-spokesperson), J.R.M. Annand, D.G. Ireland,
K. Livingston, I.J.D. MacGregor, B. McKinnon, B. Seitz, D. Sokhan
University of Glasgow, Glasgow, Scotland

S. Širca (co-spokesperson), J. Beričič, M. Mihovilovič, S. Štajner
J. Stefan Institute and Dept. of Physics, University of Ljubljana, Ljubljana, Slovenia

B. Wojtsekhowski (spokesperson-contact), A. Camsonne, S. Covrig,
P. Degtiarenko, R. Ent, D. Gaskell, D. Higinbotham, M.K. Jones,
C. Keppel, V. Kubarovksy, P. Nadel-Turoński, B. Sawatzky,
P. Solvignon, M. Ungaro, S.A. Wood, J. Zhang
Thomas Jefferson National Accelerator Facility, Newport News, VA 23606

I. Albayrak, M.A. Pannunzio Carmignotto, J. Denes-Couto,
N. Hlavin, T. Horn, F. Klein, B. Nepal
The Catholic University of America, Washington, DC 20064

S. Abrahamyan, A. Asaturyan, A. Mkrtchyan, H. Mkrtchyan,
V. Tadevosyan, A. Shahinyan, H. Voskanyan, S. Zhamkochyan
A.I. Alikhanyan National Science Laboratory, Yerevan 0036, Armenia

V. Bellini, M. Capogni, E. Cisbani, A. Del Dotto, C. Fanelli,
F. Garibaldi, S. Frullani, G. Salmé, G.M. Urciuoli
INFN, Italy

G.B. Franklin, V. Mamyan, B. Quinn
Carnegie Mellon University, Pittsburgh, PA 15213

L. El Fassi, R. Gilman, G. Kumbartzki, K. Myers, R. Ransome, Y. Zhang
Rutgers, The State University of New Jersey, Piscataway, NJ 08854

D. Nikolenko, I. Rachek, Yu. Shestakov
Budker Institute, Novosibirsk, Russia

W. Boeglin and P. Markowitz
Florida International University, Miami, FL 33199

V. Punjabi
Norfolk State University, Norfolk, VA 23504

B. Vlahovic
North Carolina Central University, Durham, NC 03824

A. Ahmidouch and S. Danagoulian
North Carolina A&T State University, Greensboro, NC 27411

A.K. Opper
The George Washington University, Washington, DC 20052

Darko Androic
University of Zagreb, Zagreb, Croatia

T. Averett and C. Perdrisat
College of William and Mary, Williamsburg, VA 23185

J. Dunne and D. Dutta
Mississippi State University, Mississippi State, MS 39762

C. Hyde, A. Radyushkin, M.N.H. Rashad
Old Dominion University, Norfolk, VA 23529

D. Day, R. Lindgren, D. Keller, N. Liyanage, B. E. Norum, O. Rondon
University of Virginia, Charlottesville, VA 22901
and
The Neutral Particle Spectrometer collaboration:
`https://wiki.jlab.org/cuawiki/index.php/Collaboration`

May 5, 2013

NEUTRAL PARTICLE SPECTROMETER (NPS) COLLABORATION

A. Camsonne, R. Ent, P. Nadel-Turoński, S.A. Wood, B. Wojtsekhowski
Jefferson Lab, Newport News, VA 23606

A. Asaturyan, A. Mkrtchyan, H. Mkrtchyan, V. Tadevosyan,
S. Zhamkochyan
A.I. Alikhanyan National Science Laboratory, Yerevan 0036, Armenia

M. Guidal, C. Munoz Camacho, R. Paremuzyan
Institut de Physique Nucleaire d'Orsay, IN2P3, BP 1, 91406 Orsay, France

I. Albayrak, M. Carmignotto, J. Dénes-Couto, N. Hlavin, T. Horn
F. Klein, B. Nepal
The Catholic University of America, Washington, DC 20064

C. Hyde, M.N.H. Rashad
Old Dominion University, Norfolk, VA 23529

P. King, J. Roche
Ohio University, Athens, OH 45701

D. Day, D. Keller, O. Rondon
University of Virginia, Charlottesville, VA 22901

D. Hamilton
University of Glasgow, Glasgow, Scotland, UK

S. Sirca
University of Ljubljana, Ljubljana, Slovenia

Contents

Abstract

We propose an experiment to measure the cross-section for real Compton scattering from the proton at an incident photon energy of 8 GeV (s = 15.9 (GeV/c)^2) and 10 GeV (s = 19.6 (GeV/c)^2) in a broad span of scattering angles ranging from $\theta_{\rm cm} = 40^\circ$ to 120°.

The JLab RCS experiment, E99-114, demonstrated the feasibility of the experimental technique and produced remarkable results. Namely, the cross section measurement made during E99-114, much more precise than the first experiment at Cornell, revealed a strong disagreement with the pQCD scaling prediction in the 6-GeV energy regime, but indicated that the reduced cross section could be described by a single form factor. It was also observed during E99-114 that at s= 7 (GeV/c)^2 and $\theta_p^{cm} = 120^\circ$, the longitudinal polarization is in agreement with the handbag description of the process in which the photons interact with a single quark, but is completely inconsistent with a pQCD mechanism which involves three active quarks interacting by two hard gluon exchanges. It is essential to have additional cross section measurements at higher photon energy over a broader kinematic range in order to identify the reaction mechanism and try to establish whether the factorization regime has been attained.

The proposed experiment utilizes an untagged bremsstrahlung photon beam and the standard cryogenic liquid hydrogen target. The scattered photon is detected in the NPS photon spectrometer, proposed for construction in Hall C. The electron beam will pass through the liquid hydrogen target, with scattered electrons being deflected by a small magnet to allow discrimination between the elastic photon and the elastic electron scattering processes. The recoil proton will be detected in the Hall C magnetic spectrometer HMS. **With 1000 hours of beam time, high precision data at the highest photon energies will be obtained.**

Such a measurement would be of crucial importance for the understanding of the reaction mechanism for this the simplest process involving a real photon, and provide an essential foundation for the understanding of other photo-induced exclusive reactions in the JLab energy range. These RCS data will also be essential in the analysis of the two photon exchange effects in elastic electron-nucleon scattering.

1 Introduction

Compton scattering in the hard scattering limit is a powerful probe of the structure of the nucleon. Compton scattering in the wide angle regime, WACS, provides access to the high-t transverse structure of the hadron, while in the DVCS regime it provides access to the high-Q^2 low-t structure. It is a natural complement to other exclusive reactions, such as high-Q^2 elastic electron scattering and high energy meson photo-production. Two-photon coupling to the hadron allows access to structure information which is not available from DIS and could be important in elastic electron scattering; at the same time data on the RCS process is likely to be more suitable for theoretical analysis than other more complex photo-induced reactions.

Very recently three new theoretical papers relevant to WACS were published. The calculations of two-photon effects in the soft-collinear effective theory, SCET, which has proved factorization of the handbag mechanism to the hard and soft contributions, were made by N. Kivel and M. Vanderhaeghen [1]. The SCET theory also provided a phenomenological analysis of the WACS observables. The SCET formula for the WACS cross section is very similar to the one in the handbag approach [2, 3, 4]. The GPD-based analysis of the electron-nucleon scattering form factors and WACS was updated by M. Diehl and P. Kroll with a refined prediction of the high energy WACS cross section and its form factors [5]. The formalism of the RCS theory based on the Dyson-Schwinger Equation (DSE) approach has very recently been proposed by G. Eichmann and C. Fisher [6]. The specific results for the WACS observables are not yet published. However, considering the advance of the elastic electron-nucleon form factor calculation achieved in the DSE approach [7, 8], the perspective of a microscopic theory of WACS in the near future looks very promising.

For real photon Compton scattering, the hard scale is achieved when s, $-t$, and $-u$ are all large compared with the proton mass or, equivalently, when the transverse momentum transfer $p_\perp$ is large (the WACS regime). Under such conditions one expects the transition amplitude to factorize into the convolution of a perturbative hard scattering amplitude, which involves the coupling of the external photons to the active quarks, with an overlap of initial and final soft (nonperturbative) wave functions, which describes the coupling of the active quarks to the proton. Schematically this can be written as

$$T_{if}(s,t) \;=\; \Psi_f \otimes K(s,t) \otimes \Psi_i \,, \tag{1}$$

where $K(s,t)$ is the perturbative hard scattering amplitude, and the Ψ's are the soft wave functions. Different factorization schemes have been applied to RCS in recent years and these can be distinguished by the number of active constituents participating in the hard scattering subprocess. The handbag mechanism [2, 3, 4, 5] involves only one active constituent, while the perturbative QCD (pQCD) mechanism [9, 10, 11, 12, 13] involves three. In any given kinematic regime, both mechanisms will contribute, in principle, to the scattering amplitude. At "sufficiently high" energy the pQCD mechanism is expected to dominate, but it is not known how high is sufficiently high or the manner in which the transition to the purely pQCD mechanism emerges.

At relatively low energy (e.g. in the resonance region), RCS and other exclusive reactions are dominated by purely soft physics, and the amplitude does not factorize into hard and soft processes. At high energy but small $-t$ or $-u$, soft physics also dominates through Regge exchanges [28]. The nature of the transition from purely soft to the factorization regime is not well known. Quite aside from the reaction mechanism, it is of interest to ask what RCS can teach us about the nonperturbative structure of the proton and to relate it to that revealed in other reactions.

With this backdrop, experiment E99-114 [14] was undertaken to study the RCS reaction. The primary focus was the measurement of precise spin-averaged cross sections over the kinematic regime of $5 \leq s \leq 11$ (GeV/c)^2 and $1.5 \leq -t \leq 6.5$ (GeV/c)^2. The measurement has produced the important result [15] shown in Fig. 1, and which will be discussed in more detail in the next section of this proposal.

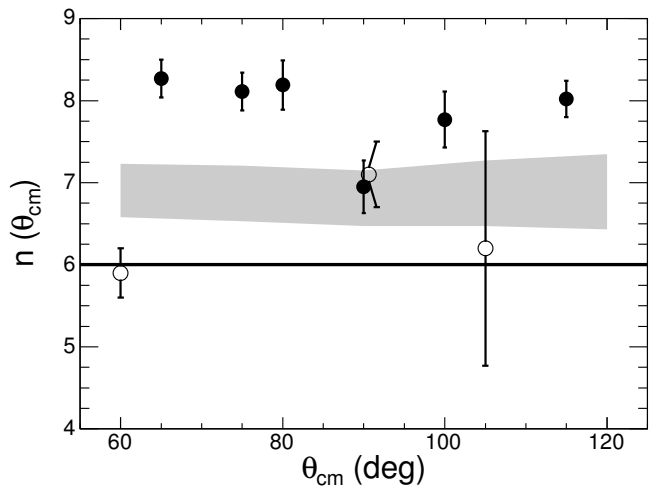

Figure 1: Scaling of the RCS cross section at fixed θ_{CM}. Full symbols denote the data from the E99-114 experiment [15]. The solid line corresponds to a constituent counting rule and scaling with fixed value $n = 6$. Open symbols denote the data from the Cornell experiment [16]. The gray band shows the range allowed by the GPD-based calculations according to [4].

In addition, a measurement was made at a single kinematic point of the polarization transfer to the recoil proton by using longitudinally polarized incident photons. The latter measurement has produced a remarkable result [17], shown in Fig. 2. Namely, the longitudinal polarization transfer is consistent with the handbag and Regge exchange predictions, while it is completely inconsistent with predictions based on pQCD. This gives very strong credence to the notion that — at least in this energy range — the photons interact with a single quark. Indeed, the longitudinal polarization is nearly as large as that expected for scattering from a free quark. However, we strongly emphasize that this is a measurement at a *single kinematic point*, and that the factorization regime might not have been reached in this case since the corresponding value of u was only -1.1 (GeV/c)^2.

These results are so intriguing that it is essential to verify E99-114 findings with measurements over a broader kinematic range, especially for higher photon energies. At 8 and 10 GeV photon energy, the factorization condition that all kinematic variables are much larger than the proton mass is unequivocally met.

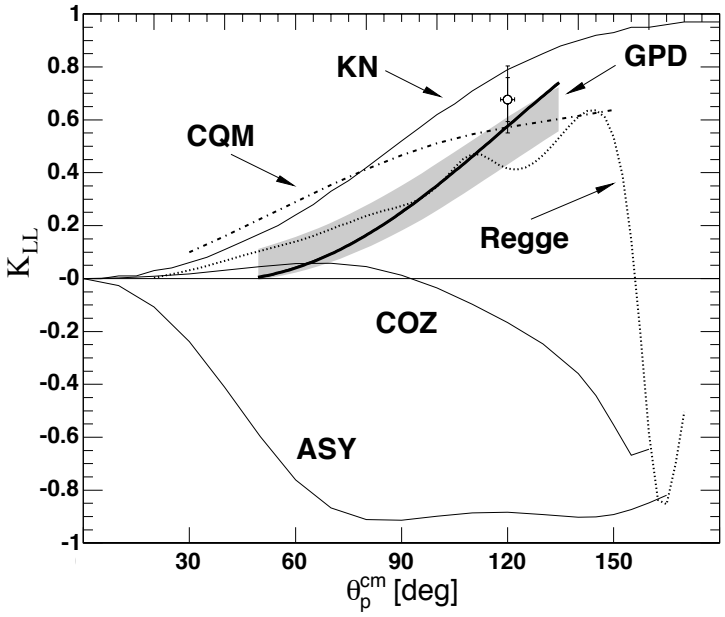

Figure 2: Longitudinal polarization transfer in the RCS process at an incident energy of 3.23 GeV [17]. The labels on the curves are KN for the asymmetry in the hard subprocess; GPD, shown as a gray band, for the handbag approach using GPD's [18]; CQM for the handbag approach using constituent quarks [19]; Regge for a Regge exchange mechanism [20]; and COZ and ASY for pQCD calculations [12] using the asymptotic (ASY) or Chernyak-Ogloblin-Zhitnitsky (COZ) distribution amplitudes.

We propose new measurements of the differential cross section in Compton scattering at incident energies of 8 and 10 GeV, or $s = 15.9$ and 19.6 $(\mathrm{GeV}/c)^2$ over a broad span of scattering angles ranging from $\theta_{\mathrm{cm}} = 40°$ to $120°$. These will constitute the first pioneering measurements ever to investigate WACS at photon energies above 6 GeV. The range of the variable t will be almost double compared with the previous experiment [14]. As the values of s, $-t$ and $-u$ will all be large, the experiment will provide a much firmer grip on the manner in which factorization is realized. Even if this answer remains elusive, the experiment will provide unique data for testing QCD based theories and an important input for two-photon exchange calculations and GPD models.

The proposal is organized as follows: In Section 2 we present our physics motivation and summarize the physics goals of the proposed experiment. In Section 3 we describe the experimental approach and both the standard and the specialized equipment. In subsequent sections, we present our proposed measurements , our expected results and beam time request (Sec. 5), and the technical considerations related to the equipment construction and the experiment schedule (Sec. 6). The proposal is summarized in Section 7.

2 Physics Motivation

In view of the remarks made in the Introduction, we consider several interesting questions that motivate us to explore further the cross section measurement in WACS at JLab:

1. Is it indeed true that the RCS reaction proceeds through the interaction of the photons with a single quark?
2. What information can be obtained about the structure of the proton from new measurements of the WACS form factor $R(t)$?
3. At what kinematic scale does pQCD scaling begin to be valid?

In the following subsections we briefly present a discussion of WACS in the pQCD limit, the soft-collinear effective theory, the handbag approach with GPD's, the DSE development for WACS, and the relativistic constituent quark model.

2.1 pQCD Mechanism

The traditional framework for the interpretation of hard exclusive reactions has been perturbative QCD (pQCD) [21]. This is based in part on the observation that the onset of scaling in Deep Inelastic Scattering (DIS) occurs at the relatively low scale of $Q^2 \sim 1$–2 (GeV/c)^2, thereby giving rise to expectations that pQCD might also be applicable to exclusive processes in the range of a few (GeV/c)^2. The pQCD approach to RCS [9, 10, 11, 12, 13] is shown in Fig. 3, where it is seen that all three valence quarks are active participants in the hard subprocess, which is effected by the exchange of two hard gluons, while the soft physics is contained in the valence quark distribution amplitudes.

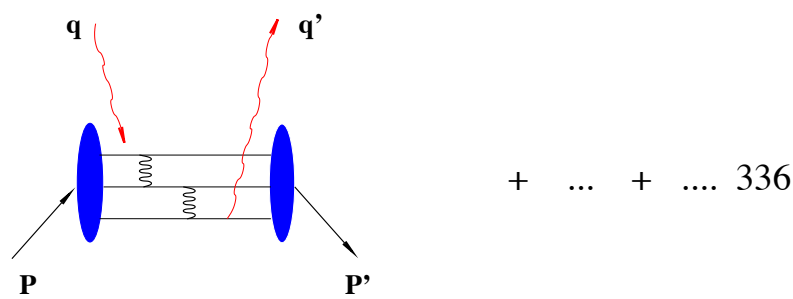

Figure 3: Two gluon exchange pQCD diagram (plus about 336 similar) for RCS.

The pQCD mechanism leads naturally to the so-called constituent counting rules for exclusive processes:

$$\frac{d\sigma}{dt} = \frac{f(\theta_{cm})}{s^n}, \tag{2}$$

where n is related to the number of active constituents in the reaction [22, 23]. Indeed, the observation that many exclusive reactions, such as elastic electron scattering, pion photoproduction, and RCS, approximately obey Eq.2 has led to the belief that the pQCD mechanism dominates at experimentally accessible energies. There seems to be little theoretical disagreement that the pQCD mechanism dominates at sufficiently high energies [24]; however, there is no consensus on how high is "sufficiently high." Indeed, despite the observed scaling, absolute cross sections calculated using the pQCD framework are very often low compared to existing experimental data, sometimes by more than an order of magnitude. Moreover, several recent JLab experiments that measure polarization observables also disagree with the predictions of pQCD. In the G_E^p experiment [25, 26] the slow falloff of the Pauli form factor $F_2(Q^2)$ up to Q^2 of 5.5 $(\mathrm{GeV}/c)^2$ provides direct evidence that hadron helicity is not conserved, contrary to predictions of pQCD. Finally, in the recently completed RCS experiment, E99-114, the preliminary analysis of the longitudinal polarization transfer K_{LL}shows a value which is large and positive, contrary to the pQCD prediction which is negative. Moreover, the E99-114 data are consistent with a scaling factor $n \approx 7.5 - 8$ rather than the value $n = 6$, which is expected from pQCD and was consistent with earlier, less precise data [16] (see Fig. 1).

A recalculation of the pQCD mechanism and reassessment in light of the E99-114 data has recently been completed by Thompson et al. [13]. It is argued in this work that K_{LL} should be measured in a regime where the kinematic variables are all significantly larger than the proton mass scale, which was not the case in E99-114. They further argue that the observed decrease in the scaled cross section as s increases is consistent with a view that the onset of the asymptotic regime will soon be accessible. Moreover, some commonality between the pQCD and handbag mechanisms has been indicated, with the suggestion that inclusion of higher twist effects will introduce the necessary proton helicity flip contributions in order to better account for available data.

The differences and similarities between precise experimental data for exclusive high-t reactions and the pQCD predictions mentioned above (see, for example, the recent analysis [27]) suggest to us a very intriguing question about the origin of the observed scaling at experimentally accessible energies:

— why the cross section $d\sigma/dt$ scales as s^{-n}, and

— why the experimental power parameter n is so close to the pQCD prediction.

Careful investigation of the WACS process could be a powerful way to discover answers to these questions.

2.2 Two-photon Physics in SCET

The soft-collinear effective theory, SCET, was developed for electron-proton scattering at large momentum transfer [1]. The QCD factorization approach formulated in the framework of SCET allowed one to develop a description of the soft-spectator scattering contribution. The two-photon exchange (TPE) corrections were calculated in the region where the kine-

matic variables describing the elastic electron-proton scattering are moderately large relative to the soft hadronic scales (M_p and Λ_{QCD}). This calculation includes the two-photon exchange contributions, TPE, to the scattering amplitude and factorizes these with a SCET form factor $\mathcal{F}_1(Q)$. The same form factor also naturally arises in wide-angle Compton scattering.

The unpolarized cross section describing Compton scattering has the form:

$$\frac{d\sigma}{dt} \simeq \frac{2\pi\alpha^2}{(s-m^2)^2}\left(\frac{1}{1-t/s}+1-t/s\right)|\mathcal{R}|^2 = \frac{d\sigma^{KN}}{dt}|\mathcal{R}|^2, \tag{3}$$

where $d\sigma^{KN}$ is the Klein-Nishina cross section corresponding to a point-like massless particle. The values $|\mathcal{R}^{exp}| = \sqrt{d\sigma^{exp}(s,t)/d\sigma^{KN}(s,t)}$ extracted from the data [15] are shown in Fig. 4 taken from Ref. [1] and show the results at three different values of the invariant mass: $s = 6.8$, 8.9 and 10.9 GeV^2 at $2.5 < -t < 6.5$ GeV^2. As one can see from this plot, the extracted values $|\mathcal{R}^{exp}|$ do not show any significant dependence on the values of s, as required by factorization. However, for the largest range of $t$the measurements are performed only at one value of s. It would be of large interest to find how this prediction works at much higher values of s over the same range of t (as proposed in this experiment).

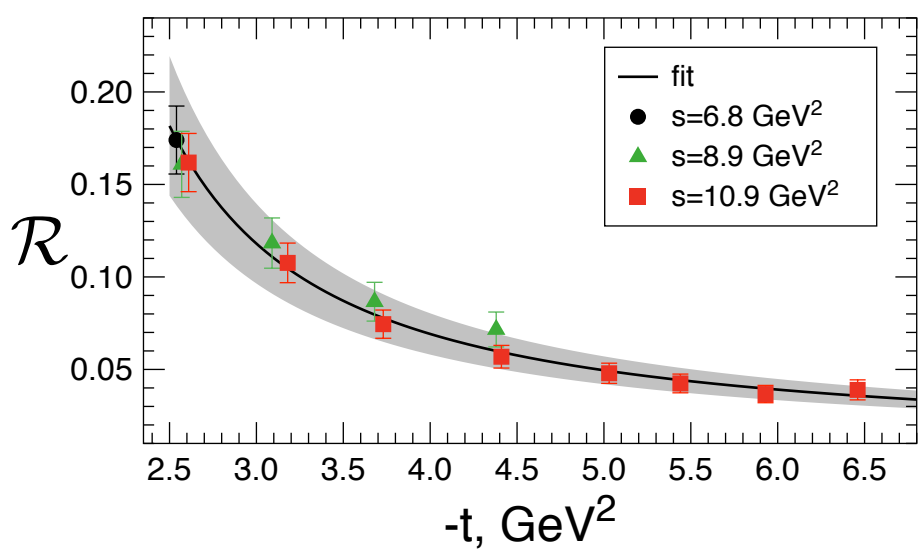

Figure 4: The ratio $\mathcal{R}$ extracted from the WACS data [15] and the fit without kinematic power corrections [1]. The gray band shows the 1σ error bands of the fit.

2.3 Handbag Mechanism and GPD-based Models

The handbag mechanism offers new possibilities for the interpretation of hard exclusive reactions. For example, it provides the framework for the interpretation of so-called deep

exclusive reactions, which are reactions initiated by a high-Q^2 virtual photon. The application of the formalism to RCS (see Fig. 5) was initially worked out to leading order (LO) by A. Radyushkin [2] and subsequently by M. Diehl and collaborators [3]. More recently next-to-leading-order (NLO) contributions have been calculated by H. Huang and P. Kroll [4].

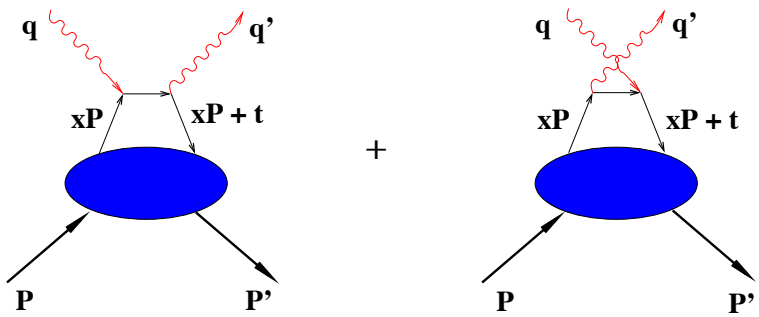

Figure 5: The handbag diagram (left) and the crossed term (right) for RCS.

The corresponding diagram for elastic electron scattering is similar to Fig. 5, except that there is only one external virtual photon instead of two real photons. In the handbag approach, the hard physics is contained in the scattering from a single active quark and is calculable using pQCD and QED: it is just Compton scattering from a structureless spin-1/2 particle. The soft physics is contained in the wave function describing how the active quark couples to the proton. This coupling is described in terms of GPD's.

The GPD's have been the subject of intense experimental and theoretical activity in recent years since the original articles [29, 30]. They represent "superstructures" of the proton, from which other measurable structure functions are derived, such as parton distribution functions (PDF) and form factors. To NLO, only three of the four GPD's contribute to the RCS process: $H(x, \xi = 0, t)$, $\hat{H}(x, \xi = 0, t)$, and $E(x, \xi = 0, t)$. Since the photons are both real, the so-called skewness parameter ξ=0, reflecting the fact that the momentum absorbed by the struck quark is purely transverse.

In the handbag formalism, the RCS observables are new form factors of the proton that are x^{-1}-moments of the GPD's:

$$
\begin{aligned}
R_V(t) &= \sum_a e_a^2 \int_{-1}^{1} \frac{dx}{x} H^a(x, 0, t), \\
R_A(t) &= \sum_a e_a^2 \int_{-1}^{1} \frac{dx}{x}\, sign(x)\, \hat{H}^a(x, 0, t), \\
R_T(t) &= \sum_a e_a^2 \int_{-1}^{1} \frac{dx}{x} E^a(x, 0, t),
\end{aligned}
$$

where e_a is the charge of the active quark and the three form factors are, respectively, the

vector, axial vector, and tensor form factors. The corresponding form factors for elastic electron or neutrino scattering are given by the x^0-moments of the same GPD's:

$$\begin{aligned} F_1(t) &= \sum_a e_a \int_{-1}^{1} dx\, H^a(x,0,t), \\ G_A(t) &= \sum_a \int_{-1}^{1} dx\, sign(x)\, \hat{H}^a(x,0,t), \\ F_2(t) &= \sum_a e_a \int_{-1}^{1} dx\, E^a(x,0,t), \end{aligned}$$

where the three quantities are, respectively, the Dirac, axial, and Pauli form factors. On the other hand, the $t = 0$ limit of the GPD's produce the PDF's:

$$\begin{aligned} H^a(x,0,0) &= q^a(x), \\ \hat{H}^a(x,0,0) &= \Delta q^a(x), \\ E^a(x,0,0) &= 2\frac{J^a(x)}{x} - q^a(x), \end{aligned} \tag{4}$$

where J^a is the total angular momentum of quark flavor a and is not directly measurable in DIS.

In the handbag factorization scheme, the RCS helicity amplitudes are related to the form factors by

$$\begin{aligned} M_{\mu'+,\mu+}(s,t) &= 2\pi\alpha_{em}\left[T_{\mu'+,\mu+}(s,t)(R_V(t)+R_A(t)) + T_{\mu'-,\mu-}(s,t)(R_V(t)-R_A(t))\right], \\ M_{\mu'-,\mu+}(s,t) &= 2\pi\alpha_{em}\frac{\sqrt{-t}}{m}\left[T_{\mu'+,\mu+}(s,t) + T_{\mu'-,\mu-}(s,t)\right] R_T(t), \end{aligned}$$

where μ, μ' denote the helicity of the incoming and outgoing photons, respectively. The signs on indices of M and T refer to the helicities of the proton and the active quark, respectively. This structure of the helicity amplitudes leads to a simple interpretation of the RCS form factors: $R_V \pm R_A$ describe the response of the proton to the emission and re-absorption of quarks with helicity in the same/opposite direction with respect to the proton helicity, and R_T is directly related to the proton helicity-flip amplitude [4].

These equations lead to expressions relating RCS observables to the form factors. The most important of these experimentally are the spin-averaged cross section and the recoil polarization observables. The spin-averaged cross section factorizes into a simple product of the Klein-Nishina (KN) cross section describing the hard scattering from a single quark and a sum of form factors depending only on t [2, 3]:

$$\frac{d\sigma/dt}{d\sigma_{\rm KN}/dt} = f_V\left[R_V^2(t) + \frac{-t}{4m^2}R_T^2(t)\right] + (1-f_V)R_A^2(t)\,. \tag{5}$$

For the interesting region of large $p_\perp$, the kinematic factor f_V is always close to 1. Consequently the unpolarized cross sections are largely insensitive to R_A, and the left-hand-side of Eq. (5) is nearly s-independent at fixed t. The recent calculations to NLO, which take into account both photon and proton helicity-flip amplitudes, do not change this prediction in any appreciable way [4]. A new analysis of the GPD's recently performed by Diehl and Kroll [5] gave an updated prediction for the WACS cross section, see Fig. 6.

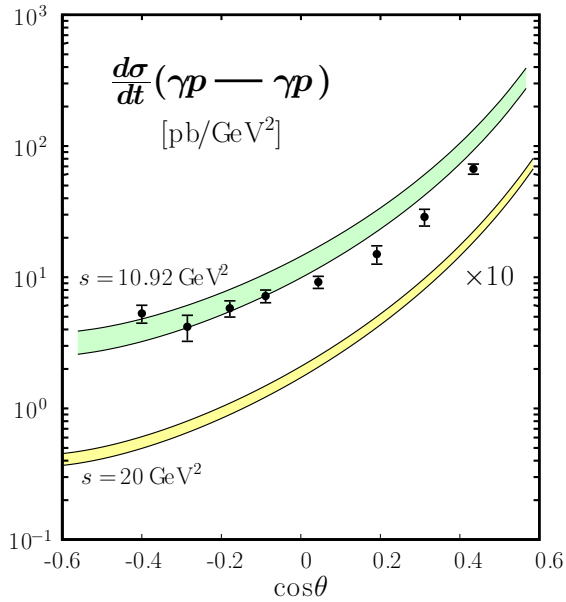

Figure 6: The GPD-based prediction for the WACS cross section [5].

2.4 Real Compton Scattering in the DSE approach

For all the insight that we gain from pQCD, we learn rather little about many of the most important issues concerning nucleon structure, such as the dynamical generation of mass through Dynamical Chiral Symmetry Breaking (DCSB), or quark confinement. There are, however, analytical techniques that at least in principle appear to have the potential to provide solutions to QCD in the non-perturbative regime with arbitrarily high accuracy. One such technique is based on the infinite tower of Dyson-Schwinger equations (DSEs) that relate the Green's functions of a field theory to each other [33]. In principle, solving the DSEs provides a solution to any field theory. In any practical calculation, however, the DSEs must be truncated, and some Ansätze must be employed to account for the omitted functions. By carefully maintaining certain properties of the theory, however, such as local and global symmetries, considerable progress can be made. Recent calculations, for instance, explicitly describe the dynamic generation of the mass of constituent quarks, and show

excellent agreement with the lattice QCD results that necessarily assume large current-quark masses. In Fig. 7 the dressed-quark mass function $M(p)$ is shown as a function of momentum for each of three bare-quark masses.

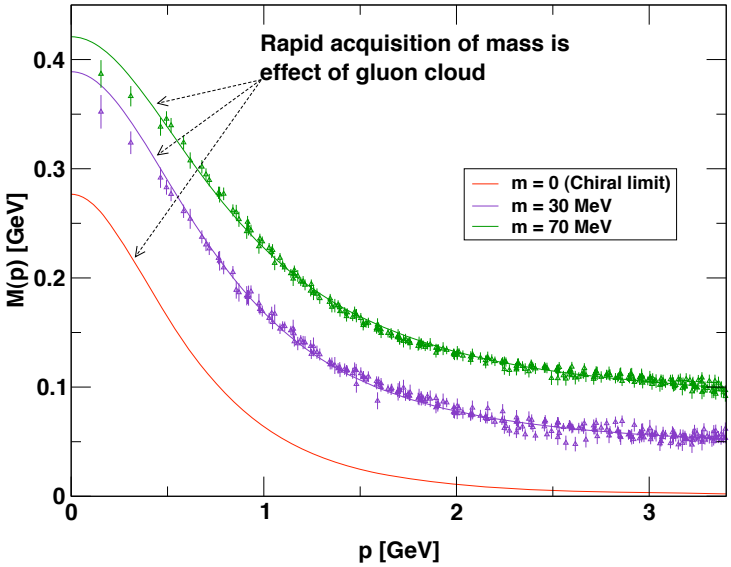

Figure 7: Dressed-quark mass function, $M(p)$. The solid curves show DSE results and the "data" represent unquenched LQCD calculations. In this figure one observes the current-quark of perturbative QCD evolving into a constituent-quark as its momentum becomes smaller.

Using dressed quarks as the elementary degrees of freedom, one can calculate nucleon form factors using a Poincaré covariant Faddeev equation, as has been done recently by C. D. Roberts and collaborators [7, 8]. These authors also assume that two of the quarks couple into a diquark. While still an approximation, the DSE/Faddeev approach is in part based on first principles. It is limited, however, in that there are precisely three (and for instance, not five) constituent quarks used as an input to the calculation. Even so, as mentioned earlier, it is reasonable to assume the dominance of the three-quark component of the wave function at relatively high values of Q^2. The DSE/Faddeev calculations provide a remarkably good description of the available elastic electron-nucleon form factor data, which is likely telling us a fairly profound fact about the nucleon's structure.

These advances in the form factors calculations lead to the expectation that the WACS process could also be calculated in the DSE approach. Indeed, in a recent paper [6] the relevant phenomenology for the RCS reaction has been developed. However, the calculations for specific observables are not yet available.

2.5 Handbag Mechanism in a Relativistic Constituent Quark Model

A different formulation for RCS in the handbag approach that differs significantly from the GPD formalism described above is that of Miller [19]. In his approach the handbag diagram involves γq scattering, as before, and proton wave functions obtained from relativistic Constituent Quark Models (CQM). What distinguishes this approach from both the Leading Order GPD and pQCD models is the fact that these proton wave functions explicitly include the influence of quark transverse momenta and configurations involving non-zero quark orbital angular momentum. This naturally corresponds to violation of proton helicity conservation. Indeed, non-conservation of proton helicity in this model has proven to be one of the key factors in its successful account of electromagnetic form factor data for the proton [31, 32].

The calculations for RCS involve evaluating the handbag diagrams of Fig. 5 in an impulse approximation. The resulting reaction amplitude depends on proton wave functions obtained from Poincaré invariant calculations involving constituent quark models in light-front dynamics. These wave functions have previously been constrained by proton electromagnetic form factor data in the same kinematic regime [32]. Significant contributions to the wave functions from quark transverse momenta and orbital angular momentum are a natural feature of the relativistic calculations.

Reasonable agreement with RCS cross section data has been obtained with a slight modification of the constituent quark masses [19]. In the case of the RCS spin observables, a similar large value of K_{LL} as for the GPD approach (see Fig.2) and a value for the transverse polarization transfer of $K_{LT}= 0$ have been predicted.

2.6 Summary of Physics Goals

We propose measurements of the cross-section for real Compton scattering at incident photon energies of 8 GeV ($s = 15.9$ (GeV/c)^2) and 10 GeV ($s = 19.6$ (GeV/c)^2) in a broad span of scattering angles ranging from $\theta_{\rm cm} = 40°$ to $120°$. The specific physics goals are as follows:

1. To provide the first determination of the WACS cross section at photon energies of 8 and 10 GeV, which is significantly above the kinematic range of any previous experiment, almost doubling the range of t.

2. To measure the cross section scaling parameter at fixed θ_{cm} for s up to 19.6 (GeV/c)^2.

3. To measure the WACS form factor, and thereby test predictions of the SCET- and GPD-based calculations.

The overall statistical precision with which we will address these physics goals will be discussed in Sec. 5.

3 Experimental Setup

The configuration of the experimental setup is similar to the one used in the E99-114 (Hall A RCS [14]) and in the E07-002 (Hall C RCS [34]) experiments. The recoil protons will be detected in the High-Momentum Spectrometer (HMS) in standard configuration. The Compton-scattered photons will be detected by the Neutral Particle Spectrometer (see Figs. 8 and 9) which, along with other key equipment, is described in the following section.

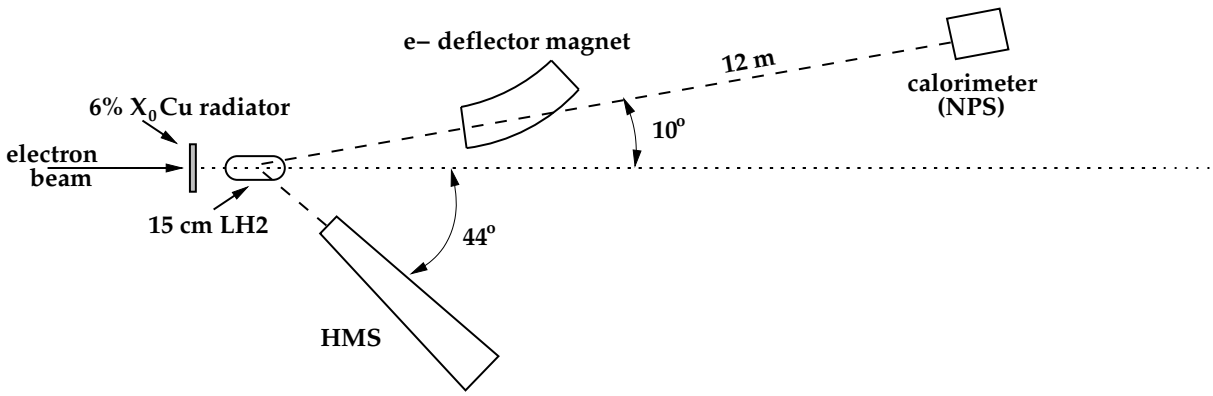

Figure 8: Schematic of the setup (kinematic 5A) at 10 GeV with the HMS detecting the recoil protons and the photon calorimeter detecting the Compton-scattered photons in addition to a fraction of elastically scattered electrons which will be partly removed by the deflector magnet. The magnet will in fact be vertically bending for reasons outlined below.

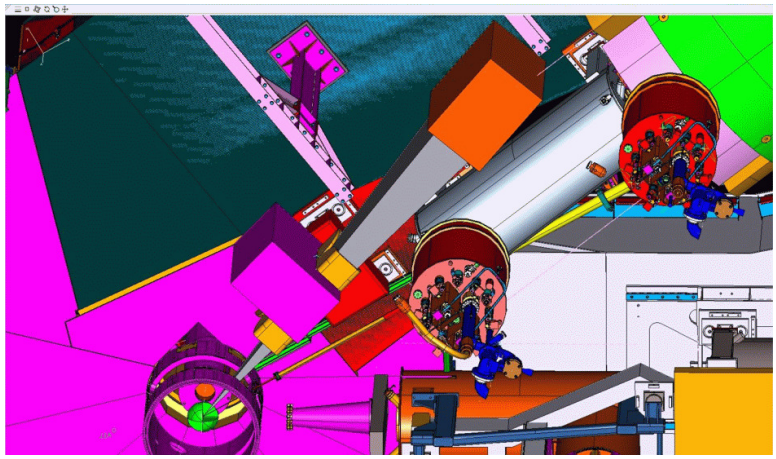

Figure 9: Proposed setup of the WACS experiment in Hall C. Looking downstream from the scattering chamber the deflection magnet, the helium bag and the calorimeter frame can be seen. The calorimeter in this configuration is located beam-left relative to the beam-pipe and on the left side of the SHMS spectrometer.

3.1 The CEBAF Electron Beam

Based on our experience with E99-114, we opt for an incident unpolarized electron beam with a current of up to 60 μA delivered in Hall C. Combined with the 10 cm long LH2 target, this implies an average luminosity of $\mathcal{L}_{\rm ep} = 1.58 \cdot 10^{38}/{\rm Hz}/{\rm cm}^2$.

3.2 The High-Momentum Spectrometer

The recoil protons in the proposed experiment will be detected by the High-Momentum Spectrometer (HMS), which is part of the standard equipment of Hall C. The HMS is a high-resolution ($\delta p/p < 10^{-3}$) magnetic spectrometer in a QQQD magnet configuration with a maximum momentum of 7.5 GeV/c and a momentum bite of 18 %. It has an octagonal input aperture with an effective solid angle coverage of approximately 6 msr and can be positioned to angles greater than 12.5°.

The detector package of the HMS consists of two vertical drift chamber packages for track reconstruction, scintillator hodoscopes for timing, as well as a gas Čerenkov counter, an aerogel Čerenkov counter, and a segmented lead-glass shower calorimeter for particle identification. If needed, the shower calorimeter could be used in the trigger.

The HMS can be tuned in parallel-to-point mode (for optimal in-plane angle accuracy) or point-to-point mode (for best vertex reconstruction). In the proposed experiment it will be used in the latter mode in which extended targets can be accommodated with a vertex reconstruction accuracy of ≈ 1 mm, and where both in-plane and out-of-plane angle measurement resolutions are about 0.8 mrad. In this proposal the SIMC simulation package was used for determination of the actual momentum and angular resolutions, which included scattering in the target material as well as reconstruction effects (see Sec. 4).

3.3 The Liquid Hydrogen Target and the Radiator

The experiment will utilize one of the standard Hall C liquid hydrogen (LH2) targets with a 10 cm-long machined cell with aluminum walls of 5 mm thickness, which has been successfully employed in many experiments at JLab. The copper radiator with a thickness of $t_{\rm rad}/X_0 = 0.06$ (6 % of radiation length) will be mounted on the cell block about 4 inches upstream of the cell entrance window. The short distance between the target and the radiator helps avoid background produced on the walls of the target and keeps the photon beam spot compact, which allows both accurate measurement of the proton momentum with the vertical bend spectrometer and operation with high luminosity. Note that in the rate simulations described later in the proposal, the effective thickness of the radiator was assumed to be slightly larger, $t_{\rm rad}/X_0 = 0.08$, due to additional radiative processes in the target and the virtual photon flux.

3.4 Deflection Magnet

It was shown in the E99-114 experiment that the deflection magnet provides an effective way to discriminate between elastic electron and photon scattering events. The magnet obviates the need for a veto detector, which in turn allows us to utilize at least ten times higher photon/electron beam intensity. The design of the magnet has been driven by a number of considerations:

- Aperture for the full size of the calorimeter;
- Value of the magnetic field for electron deflection;
- Minimum magnetic field at the beam line;
- Horizontal orientation of the magnetic field.

Additional information about the magnet design is presented in Sec. 6.

3.4.1 Choice of the Direction of Deflection

One of the key aspects in discrimination of real-Compton from background events is a reliable comparison of the expected and measured electron-proton (calorimeter-HMS) correlation. The *angular spread* of this correlation is smaller out-of-plane because it is defined only by angular resolution; in contrast, it is larger in-plane because its dominant contribution comes from the proton momentum reconstruction resolution for a given proton momentum. Typically the out-of-plane resolution relevant for the e-p correlation is twice as good as the in-plane resolution. The bending direction for elastic electrons should therefore be vertical (magnetic field horizontal) in order to minimize the required deflection of electrons and the resulting value of the field in the deflection magnet.

3.4.2 Determination of the Required Field Integral

The energies of the proposed experiment are about twice as large as those encountered in E99-114, with the consequence that the angular distribution (and the corresponding spatial distribution at some drift distance) of decay photons from photo-produced π^0 will be rather focused, resulting in a real-Compton peak superimposed on a relatively narrow distribution of π^0 decay photons. As a result the pion related contribution in the final event sample will reach 38 for the $\pm 1.5\sigma$ calorimeter hit difference cut (see Table 3 below). This means that the shape of the pion related events needs to be well understood. The role of the deflector magnet is therefore not only to separate the elastic electrons from real-Compton photons but also to relocate the electrons sufficiently far from the $\pi^0 \rightarrow 2\gamma$ events. This can be accomplished by a sufficiently strong deflector magnet. A magnet that will be able to provide a field integral of up to $\int \vec{B} \cdot \mathrm{d}\vec{l} \approx 0.6\,\mathrm{Tm}$ has been designed and will be constructed for the proposed experiment. It will be placed as indicated in Fig. 9, which shows a typical setup.

3.5 The Photon Calorimeter

This experiment is possible due to the construction of the new facility: a Neutral Particle Spectrometer [37]. This photon calorimeter will consist of a rectangular array of $1116 = 31\ (\text{hor}) \times 36\ (\text{vert})$ $PbWO_4$ crystal blocks with dimensions $2.05 \times 2.05 \times 18\,\text{cm}^3$ with their associated PMTs and high-voltage (HV) dividers, as well as the corresponding mechanical and electronics systems. Figure 10 shows an array of crystal blocks that will closely resemble the one that will be used in the proposed experiment, and is based on the HYCAL [38] detector.

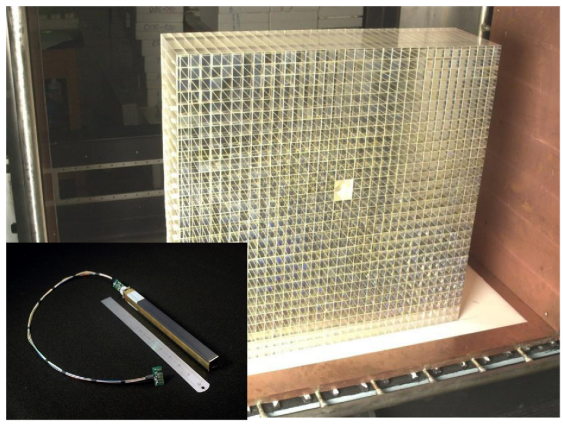

Figure 10: The high-resolution $PbWO_4$ part of the HYCAL detector on which the present calorimeter design is based.

The PMTs are shielded from ambient light in a light-tight box that contains an air-cooling system, whose main purpose is to prevent the PMTs from overheating and aid in the overall stable operation of the calorimeter. The yield of the $PbWO_4$ crystals is temperature-dependent, with $\approx -2\,\%/^\circ\text{C}$ deterioration of light yield around room temperature. HV and signal-cable systems are also contained in the light box encasing the PMTs.

The calorimeter will be equipped with a system that distributes light pulses to each calorimeter module. The main purpose of this system is to provide a quick way to check the detector operation and to calibrate the dependence of the signal amplitudes on the applied HV. The detector response to photons of a given energy may drift with time, due to drifts in the PMT gains and to changes in the glass transparency caused by radiation damage. For this reason, the gain monitoring system will also allow measurements of the relative gains of all detector channels during the experiment.

The calorimeter can be moved into the hall without being disconnected from the front-end electronics, which is located in racks a few feet behind the main detector components. The position of the photon arm will be adjusted for each kinematics to match the angular position of the HMS. The calorimeter will most likely be placed on rails and repositioned by sliding along these rails. In previous experiments less than two hours' time (beam-off to beam-on) were required to move the calorimeter in a typical hall access.

Due to radiation issues (see below) it will be very beneficial to place a 10 cm thick plastic

cover with an effective surface area thickness of approximately $10\,\mathrm{g/cm^2}$ in front of the calorimeter. This is in agreement with experience from E99-114.

3.6 Trigger of the DAQ

In contrast to E99-114, where a particular coincidence trigger scheme was used, *we will use only the HMS trigger* in this experiment. This is possible because of the modest event rate expected in the proton arm at high photon beam energies and because the new HMS and NPS electronics have practically zero dead-time, so each particle detected by the HMS will trigger the DAQ readout of both the HMS and the calorimeter. The cluster summing used in the calorimeter for E99-114 and described in [17] will therefore not be implemented in the trigger.

3.7 Effects of Radiation Load

The high luminosity required in the proposed experiment could result in loss of the energy and coordinate resolutions of the calorimeter due to pileup. Long operation at high radiation load could cause radiation damage to the crystals and loss of their performance. The radiation level in Hall C during the experiment are estimated in Sec. 6). We addressed these concerns using our experimental data from the E99-114 data taking run in 2002 and results of the Monte Carlo simulations of the rates in the NPS calorimeter [35]. The discussion is focused on kinematic 5F, for which the radiation is the largest.

3.7.1 Energy and Coordinate Resolutions

The energy of the particle detected in the calorimeter is calculated from a sum of the signals in several crystals (up to 9) which form a cluster. The noise in the ADC used for a measurement of the signal from an individual crystal contributes to the detector energy resolution. In a high-rate experiment the ADC noise is increased, and this can be characterized by the ADC pedestal width. Using the observed 5-6 MeV pedestal width in the E99-114 runs, the expected pedestal width for the 5F kinematic in the new proposal is projected to be around 50 MeV. The effect of the background on the energy resolution could be estimated from this estimated pedestal width and the number of modules in the cluster. It is expected to be on the level of 110-150 MeV or 3.3-4.5% for 5F kinematics. A similar estimate shows that the effect on the coordinate resolution is around 0.5 mm in the case of kinematic 5F and less for other kinematic settings.

An estimate of the projected counting rates of large signals in the calorimeter was also obtained from the results of E99-114 [36]. According to that study, the counting rate $f_(E_{\mathrm{thr}})$ has an exponential dependence of E_{thr}: rate $= A \times e^{-9\times E_{\mathrm{thr}}/E_{\mathrm{max}}}$, where E_{max} is the energy of an elastically scattered electron, $E_{\mathrm{beam}}/(1 + E_{\mathrm{beam}}(1 - \cos\theta)/M)$. Taking into account conditions of the current proposal (the beam current values, the radiator thickness, and the target length), we found the rates for each kinematics shown in Table 1. In off-line data

Table 1: Single rates (integrated over photon energies in the range $0.5E_\gamma^{(\max)} < E < E_{\max}$) at 60 μA beam current on a 10 cm LH2 target) with a 6% X0 radiator for settings 4A—4G ($E_e = 8.8$ GeV) and for settings 5A—5F ($E_e = 11$ GeV). The corresponding effective calorimeter solid angles for each kinematic setting have already been taken into account.

setting	4A	4B	4C	4D	4E	4F	4G
single rate [MHz]	0.9	1.2	2.2	4.3	4.8	5.2	3.9
setting	5A	5B	5C	5D	5E	5F	
single rate [MHz]	1.2	1.8	2.4	4.3	6.2	12.5	

analysis, a timing cut of ±(4-5) ns will be applied. This will bring the accidental hit probability in the HMS trigger defined events to a level below 10%, a background contribution which could be taken into account using statistical type analysis without a significant loss of the cross section determination accuracy. The GEANT4 MC simulation of the calorimeter counting rate, performed for the conditions of the 5F kinematics, results in 1.7 MHz (integrated over photon energies in the range $0.5E_\gamma^{(\max)} < E < E_{\max}$), which is as expected much lower than the rate shown in Table 1 due to a conservative approach taken in interpolation of the E99-114 results.

4 Proposed Measurements

The differential cross section for Wide-Angle Compton scattering will be determined at photon energies of 8 and 10 GeV over a wide range of -t, allowing for determination of the dominant reaction mechanism and extraction of information on the non-perturbative structure of the proton. The following subsections set out the proposed kinematic settings, the Monte Carlo simulation of the detector systems, the expected rates for RCS and background events and finally a discussion of systematic uncertainties.

4.1 Kinematic Settings

Kinematic variables for two standard beam energies of 8.8 GeV (4-pass) and 11 GeV (5-pass) over a wide range of -t have been calculated and are summarized in Table 2. The variables in the table correspond to a range of incident photon energies of 7.5 - 8.5 GeV for the 4-pass setting and 9.3 - 10.7 GeV for the 5-pass setting. In order to demonstrate the range of s and -t covered by the proposed measurements, the distribution of RCS events for recoil protons that lie within the HMS acceptance is shown in Figure 11.

	E_{in} [GeV]	θ_γ [°]	E_γ [GeV]	θ_p [°]	p_p [GeV/c]	Θ_{CM} [°]	s $[(GeV/c)^2]$	-t $[(GeV/c)^2]$	-u $[(GeV/c)^2]$
4A	8.0	11	6.917	47.47	1.791	45	15.9	2.03	12.10
4B	8.0	15	6.199	38.57	2.574	58	15.9	3.38	10.77
4C	8.0	19	5.463	32.10	3.347	71	15.9	4.76	9.37
4D	8.0	28	4.004	22.83	4.844	93	15.9	7.50	6.63
4E	8.0	33	3.368	19.51	5.491	103	15.9	8.70	5.44
4F	8.0	40	2.671	16.09	6.196	114	15.9	10.00	4.13
4G	8.0	48	2.094	13.27	6.780	124	15.9	11.08	3.05
5A	10.0	10	8.607	44.44	2.135	45	19.6	2.62	15.30
5B	10.0	14	7.596	34.94	3.208	60	19.6	4.51	13.37
5C	10.0	18	6.572	28.44	4.264	74	19.6	6.43	11.45
5D	10.0	24	5.205	21.98	5.656	90	19.6	9.00	8.89
5E	10.0	30	4.119	17.75	6.754	103	19.6	11.04	6.85
5F	10.0	36	3.295	14.79	7.586	114	19.6	12.58	5.30

Table 2: Kinematic variables for seven settings with a 4-pass beam (4A - 4G) and six settings with a 5-pass beam (5A - 5F).

These kinematic settings have been chosen in order to cover a broad range of momentum transfer in the wide-angle regime, for which the Mandelstam variables s, $-t$ and $-u$ are all unequivocally larger than the typical hadronic mass scale. In all cases, the scattering angles and momenta fall well within the respective acceptances of the HMS and NPS and pose no practical difficulties in terms of positioning of the detector systems with respect to the outgoing beam-line. The incident energy range for each setting has been selected to reach as high an incident photon energy as possible and cover a reasonably narrow range in s, while also maintaining a high event rate.

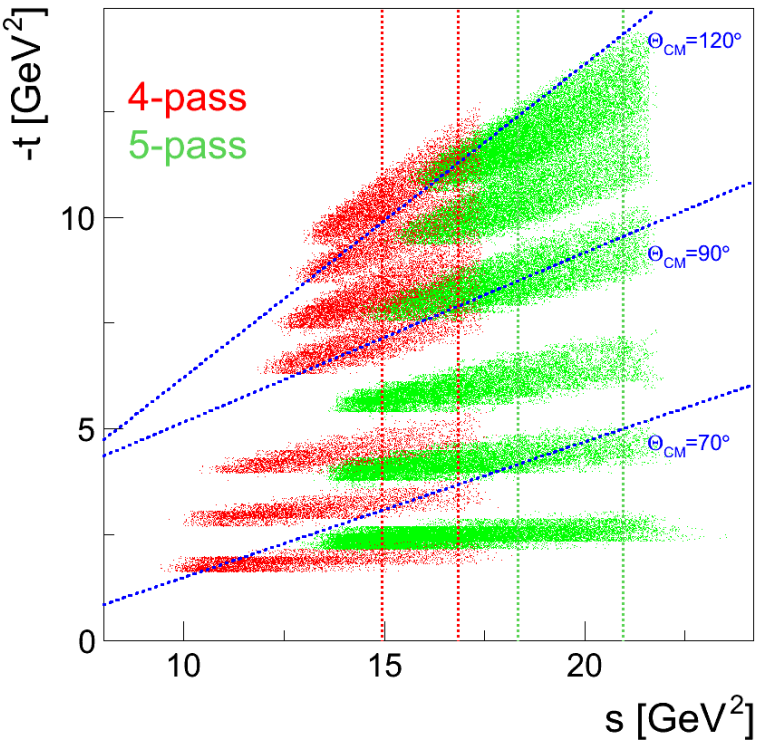

Figure 11: Range of s and -t accessible for the proposed kinematic settings as defined by the HMS acceptance (calculated in SIMC). The vertical dash lines correspond to the range of incident photon energies over which the analysis is performed.

4.2 Monte Carlo Simulation

A Monte Carlo simulation has been developed in order to study the manner in which the particles associated with the dominant physics processes will interact in the target and detector systems. Events are first generated over a much broader kinematic range than the detector acceptances according to cross section parameterizations of the three reaction types: RCS, neutral pion photoproduction, and elastic ep scattering. The parameterizations are based on E99-114 data in the case of RCS and neutral pion photoproduction [15] and the Bosted fit to the Sachs form factors for elastic ep scattering events [40]. The proton interactions in the target and HMS are then simulated using the standard Hall C SIMC simulation package, while the particles scattered towards the NPS (photons, pions and electrons) are simulated using dedicated software developed within the CERN Geant4 framework. This latter tool includes a realistic simulation of the target, scattering chamber, deflection magnet and NPS.

Experience gained during Jefferson Lab experiments E99-114 and E07-002 has allowed for the development and refinement of a technique for identifying RCS events and extracting the associated yield. The technique is relatively straightforward: One assumes two-body

kinematics and uses the measured recoil proton variables to reconstruct a predicted hit position for the corresponding scattered photon at the NPS. The differences between the predicted and measured NPS hit positions, δx and δy, are then used to identify the reaction from which a particular event originated. Figure 12 shows typical distributions of these hit difference variables from the Monte Carlo simulation (for kinematic setting 4D).

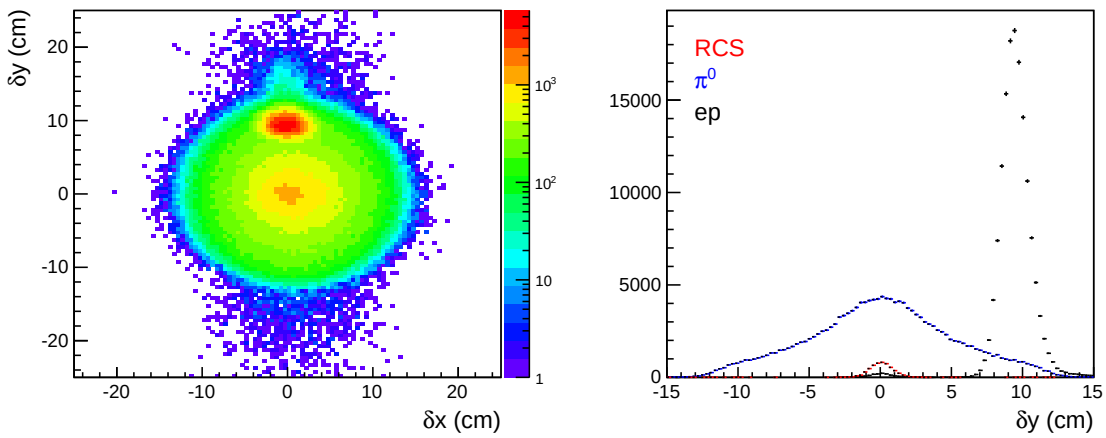

Figure 12: Typical NPS hit difference distributions for kinematic point 4D. Left: δx vs δy for all events. Right: a projection onto the δy axis for events in the central δx region.

The distributions shown in Figure12 correspond to the difference between the expected NPS hit positions for a good proton track in the HMS and the center-of-gravity positions of the highest energy NPS cluster. One can see that the elastic ep events are centered at positive δy due to deflection in the magnet, RCS events are centered around zero, and events from detection of one of the photons from the decay of a neutral pion form a relatively broad background. Although it is difficult to see for this particular kinematic setting, there is also a non-negligible background contamination in the RCS peak as a result of elastically scattered electrons which radiate in the target or scattering chamber. These so-called $ep\gamma$ events are kinematically indistinguishable from RCS events, but can be corrected for in the final yield extraction.

The free parameters associated with the experimental set-up – i.e. the deflection magnet distance and field integral, as well as the NPS distance – have been optimized with the Monte Carlo simulation for all kinematic settings in order to achieve as clean an extraction as possible of the RCS events. This involves simultaneous optimization of the resolution of the NPS hit difference distributions, the electron deflection, the relative number of background events and the RCS event rate. This process is described in more detail in the following subsections.

4.2.1 Detector Resolution

There are two features that have been established in previous JLab WACS experiments concerning the two-arm resolution for the calorimeter hit difference distributions:

- The resolution is dominated by proton multiple scattering and reconstruction in the proton spectrometer;
- The out-of-plane (δy) resolution is much better than the in-plane (δx) resolution, as a result of the fact that the latter includes significant contributions from the proton momentum and vertex resolutions.

These facts, combined with the requirement for a clear separation between RCS and elastic ep events, are the reason that a horizontal magnetic field, and therefore vertical deflection, is critical to the success of the proposed measurements.

Typical values for the expected NPS position and energy resolutions have been included in the simulation, as have photon/electron interactions in the target, scattering chamber and a 10-cm plastic shield directly in front of the NPS which acts as a shield from low-energy electromagnetic background. These result in a contribution to the resolution over all kinematic settings of around 0.35 cm. For the range of proton momenta considered in the present proposal (1.791 - 7.586 GeV/c), the in-plane and out-of-plane HMS angular resolutions, as well as the HMS momentum resolution, have also been calculated. The in-plane angular resolution varies between 1.5 and 2.5 mrad, the out-of-plane resolution between 1.7 and 3.8 mrad, and the $\delta p/p$ resolution between 5 and $7.5{\cdot}10^{-4}$. It is primarily the last (although there is a small contribution from the vertex resolution) that leads to the δx resolution being poorer than the δy resolution as a result of the two-body kinematic reconstruction.

The NPS distance clearly plays a crucial role in determining the final values for the two-arm resolutions. It has therefore been optimized for all kinematic settings such that the out-of-plane resolution remains around or less than 1 cm. Anything larger would make extraction of the RCS signal from the pion background prohibitively difficult, leading to a large systematic uncertainty.

4.2.2 Physics Background

As mentioned previously, separation of the elastic ep scattering background is achieved through the use of a deflection magnet between the scattering chamber and the NPS. In order for the separation in the out-of-plane calorimeter hit difference distribution to be sufficient for there to be no contamination under the RCS peak from these background events, a deflection corresponding to greater than 5σ is necessary. This has been achieved by choosing appropriate values for the magnet distance and the field integral for each of the kinematic settings. While it would be possible, at least for a few of the kinematic settings, to deflect the electrons outside of the NPS acceptance, this is not desirable as a result of the need to fully understand and measure the post-scattering $ep\gamma$ events. The Monte Carlo

simulation has shown that the ratio $N_{ep\gamma}/N_{RCS}$ within a region of δx -δy space of 1.5σ centered on the RCS peak varies over all kinematic settings between 0.1 (at high -t) and 2.5 (at low -t). Experience has shown that a combination of good calorimeter energy resolution and two-cluster analysis of these events, in addition to a Monte Carlo simulation, allows accurate determination of the ratio $N_{ep\gamma}/N_{RCS}$.

Detection of one or both photons from the decay of a neutral pion leads to the dominant background in the proposed measurement. The key to extraction of the RCS signal from the pion background events on which they sit is to have as full an understanding as possible of the shape of these background events. It is then relatively straightforward to employ a mix of empirical fits and Monte Carlo simulated data to fit the pion and RCS distributions and extract the RCS yield. For this reason, one other critical factor in the final values chosen for the NPS distance has been to ensure that the distribution of pion events in δx and δy is not artificially truncated by the NPS acceptance. The ratio N_{π^0}/N_{RCS} in the same 1.5σ central δx -δy region as determined in the simulation varies between 0.3 (at low -t) and 38 (at high -t), For kinematic settings for which the ratio N_{π^0}/N_{RCS} is large, reconstruction of the pion from detection of both decay photons can be used in the analysis to significantly reduce this ratio. It has been shown in studies with the simulated data and with data from previous experiments that this ratio can be precisely determined.

4.2.3 Optimization of Photon Arm Parameters

Taking into account the considerations discussed in the previous subsections, while also trying to match the HMS and NPS acceptances in order to maintain as high an RCS event rate as possible, the simulation has been used to give the optimal values for the NPS and magnet distance and the field integral, taking into account both space constraints in the experimental hall and what can be achieved with the proposed magnet design. These are given in Table 3 for all kinematic settings, together with the expected resolutions in δx and δy, the mean electron deflection and the background ratios for $ep\gamma$ and π^0 events in the central 1.5σ δx -δy region.

4.3 Expected Rates

The expected RCS event rate for the kinematic settings given in Tables 2 has been calculated with the Monte Carlo simulation and yield extraction analysis technique described above. The event rate is the product of the luminosity, the cross section, and the acceptances of the detectors, as well as all other factors such as DAQ dead time, efficiency of the trigger, and the detectors and efficiency of the reconstruction analysis. The rate N_{RCS} was calculated according to:

$$N_{RCS} = \frac{d\sigma}{dt}_{RCS} \frac{(E_\gamma^f)^2}{\pi} \Delta\Omega_\gamma f_{\gamma p} \left(\frac{\Delta E_\gamma^f}{E_\gamma^f} \frac{t_{rad}}{X_o}\right) \mathcal{L}_{ep}$$

	D_{NPS} [m]	D_{mag} [m]	$\int B \cdot dl$ [Tm]	σ_x [cm]	σ_y [cm]	e defl [cm]	N_{π^0}/N_{RCS}	$N_{ep\gamma}/N_{RCS}$
4A	11.0	2.45	0.25	5.35	1.07	9.12	0.34	1.23
4B	9.0	2.45	0.3	3.86	1.05	9.18	0.96	1.34
4C	6.0	1.65	0.35	2.41	0.84	7.93	1.93	0.51
4D	3.5	1.1	0.6	1.42	0.81	9.50	7.98	0.28
4E	3.0	1.1	0.6	1.29	0.86	8.54	15.0	0.14
4F	2.5	1.1	0.6	1.15	0.98	7.28	22.5	0.11
4G	2.5	1.1	0.6	1.32	1.11	7.97	38.3	0.13
5A	12.0	2.45	0.25	5.85	0.82	8.20	0.43	2.53
5B	9.0	2.45	0.35	3.29	0.91	8.76	1.32	1.51
5C	7.0	1.65	0.4	2.42	0.94	9.24	3.22	0.74
5D	4.5	1.65	0.5	1.65	0.89	7.48	9.83	0.34
5E	3.25	1.1	0.6	1.33	0.85	8.10	20.0	0.19
5F	2.75	1.1	0.6	1.27	0.98	7.25	36.07	0.11

Table 3: Distances from the target center for the NPS and the deflection magnet, the required field integral and the expected resolutions, background ratios and mean electron deflection.

where $\frac{d\sigma}{dt}_{RCS}$ is the RCS cross section; the factor $\frac{(E_\gamma^f)^2}{\pi}\Delta\Omega_\gamma$ is the range of Δt for the given kinematics, expressed through the energy of the scattered photon and the solid angle of the photon detector; $f_{\gamma p}$ is the fraction of events detected for a given range of photon energy E_γ^f; $(\frac{\Delta E_\gamma^f}{E_\gamma^f}\frac{t_{rad}}{X_o})$ is the number of photons per incident electron, including the photons produced in the target and virtual photons; and $\mathcal{L}_{ep}$ is the electron-proton luminosity for a given beam current.

The raw singles rates in the HMS and NPS have been determined for events arising from RCS, elastic ep scattering and π^0 photoproduction reactions. For completeness, and to determine whether additional particle identification will be needed, the HMS singles rates for π^+ photoproduction have also been calculated. These are shown for a corresponding electron beam current chosen for each kinematic setting in Table 4. The simulated HMS trigger rate is highest at low -t due to a sharp increase in the elastic ep scattering cross section. However, for all settings the HMS trigger rate will be well within acceptable HMS operating parameters as determined in previous HMS experiments. The π^+ rates are such that rejection of these events off-line via the kinematic reconstruction technique described in previous sections will be sufficient, without the need for any additional particle identification.

4.4 Systematic Uncertainties

The three main sources of systematic uncertainties in the proposed measurement of the RCS cross section are those associated with the RCS yield extraction, the determination of the detector acceptance and efficiencies, and the determination of the total photon beam flux. As before, extensive experience gained during the E99-114 and E07-002 experiments in combination with the Monte Carlo simulation studies detailed in the previous section is relied

	I_{beam} [μA]	R^{p}_{HMS} [Hz]	$R^{\pi^+}_{HMS}$ [Hz]	$R^{e^-}_{NPS}$ [Hz]	R^{γ}_{NPS} [Hz]	N_{RCS} [h^{-1}]
4A	6	200	1	600	30	340
4B	15	65	1.5	150	30	150
4C	30	30	5	90	85	160
4D	60	18	12	25	225	100
4E	60	16	13	9	210	70
4F	60	14	13	3	200	45
4G	60	8	7	1	100	25
5A	15	350	1	725	20	225
5B	30	4	1	60	7	110
5C	40	14	1	30	14	60
5D	60	7	4	20	30	40
5E	60	6	5	2	37	25
5F	60	5	5	1	35	15

Table 4: Expected physics singles rates for different particle types in the HMS and NPS detector systems. The beam current has been optimized for each of the kinematic settings. The last column shows the expected rates for RCS events.

upon to make estimates of these various sources of systematic uncertainties. Adding the various contributions described below in quadrature, it is estimated that the total systematic uncertainty for the proposed measurement will be around 8 % for the least favorable kinematic setting.

Beginning with the total photon beam flux, there are contributions to this particular uncertainty from measurement of the accumulated electron beam charge, target thickness, and determination of the bremsstrahlung photon flux for a given energy range. This last dominates, while the others are estimated to be less than 1%. The utilization of redundant calculations of the bremsstrahlung flux (using both Geant4 and dedicated thick-target bremsstrahlung tools) and measurements using the actual data lead to confidence that this uncertainty can be kept around the 3% level. Furthermore, previous experience working with the HMS, the simple geometry of the NPS, and the fact that the HMS will be operating well within its capabilities lead to the expectation that the systematic uncertainty associated with detector acceptances and efficiencies will be around the same 3% level.

The extraction of the RCS yield is subject to uncertainties from both the π^0 and $ep\gamma$ backgrounds, which vary relative to each other for different kinematic settings. In order to estimate the magnitude of the systematic errors arising as a result of contamination from these background sources (as given by the ratios in Table 3), the Monte Carlo simulated data was analyzed according to the technique developed for E99-114. The yield extracted by this technique for RCS events was then compared with the known simulated yield. It was found that, without much optimization of the procedure, one could get the differences between the extracted and simulated RCS yield taking into account the background contamination to around 94% agreement. It is expected that this level of agreement can be further improved

upon. However, there is one important caveat which relates to the strong correlation between the magnitude of this uncertainty and the total sample of RCS events. It requires a minimum of around 2,500 RCS events for the kinematic settings where the backgrounds are large. Therefore, this number of 2,500 is taken to be the required yield used in the beam-time request given in the next section.

5 Beam-Time Request and Expected Results

The number of hours of beam-time required to achieve a 10% combined uncertainty (2% statistical and 8% systematic, the latter defined primarily by the pion background dilution) on the RCS cross section for all kinematic settings has been estimated and is summarized in Table 5. These numbers have been calculated based on the expected rates given in the previous section and include estimated overheads from sources such as accelerator downtime, DAQ dead-time, detector inefficiencies and configuration changes between kinematic settings. In total, the beam-time estimate for the seven different 4-pass kinematic settings (4A–4G) is 430 hours, and 570 hours for the six 5-pass settings (5A–5F). As with E99-114, on-line analysis during the data-taking will allow for real time optimization of the required running time for each kinematic setting.

	4A	4B	4C	4D	4E	4F	4G	Total
time [h]	30	30	30	40	60	90	150	430

	5A	5B	5C	5D	5E	5F	Total
time [h]	30	30	60	90	150	210	570

Table 5: Breakdown of beam-time estimate for each of the kinematic settings, based upon the requirement of achieving a combined uncertainty of 10% on the final cross section results and implicitly including time for overheads.

The corresponding expected cross section results are shown in Figure 13, with results from the previous Jefferson Lab E99-114 experiment also included. One obvious feature of this figure is the degree to which the proposed cross section measurements will extend to a new and uncharted range in $-t$. This clearly has implications in terms of improving our understanding of the reaction mechanism and proton structure information accessible through wide-angle Compton scattering. In order to demonstrate the effect of these implications, the expected cross section results have been employed to calculate the Compton form factor $\mathcal{R}$ and the scaling power n, which were introduced in Section 2.2. The expected accuracy that can be obtained for these two important quantities based on extrapolated E99-114 results and the precision expected from the proposed series of measurements can be seen in Figure 14.

It is clear from the top plot of Figure 14 that the expected precision achievable with the proposed series of measurements will allow for an accurate and unambiguous test of factorization in WACS through examining the scaling of the form factor $\mathcal{R}$ with s. Moreover, the precision achievable in the determination of n at fixed θ_{CM}, as seen on the top of the same figure, will be sufficient to make definitive conclusions concerning the WACS reaction mechanism and whether the transition to the perturbative regime has been achieved. These results will also help explain the curious fact that the value of n determined in E99-114 drops significantly at $\theta_{CM} = 90°$, a fact that has been the topic of speculation for some years.

Finally, it should be noted that the proposed experiment will allow for the measurement of the π^0 photoproduction differential cross section to a very high degree of statistical precision. This, like WACS, has also never been measured in this high-s, wide-angle regime. The

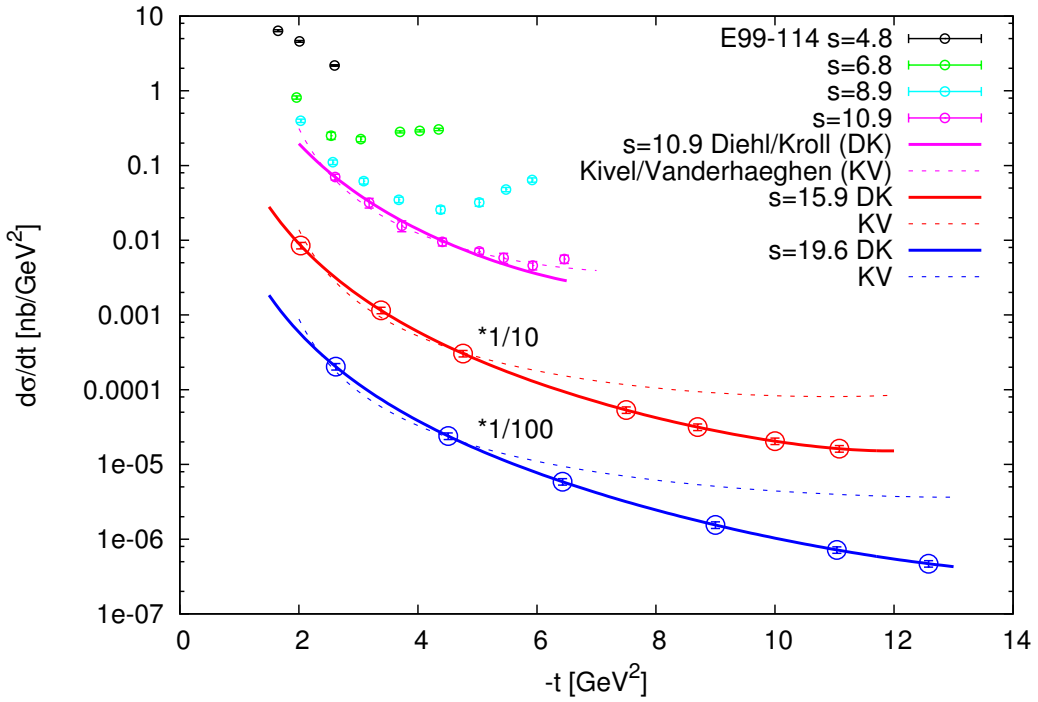

Figure 13: The anticipated data points of the proposed experiment at $s = 15.9\,\mathrm{GeV}^2$ (black symbols) and at $s = 19.6\,\mathrm{GeV}^2$ (blue symbols), together with the existing cross-sections from E99-114 [15], for the total beam time of 1000 hours. The expected points are drawn on the curves (black and blue) obtained by extrapolating the E99-114 cross-sections, which differ from the recent prediction by Diehl and Kroll [5] only at large t. The error bars are combined statistical and systematic.

information on reaction mechanisms and proton structure that can be accessed in this channel is complementary to other hard exclusive reactions such as WACS and elastic electron-nucleon scattering. Analysis of the π^0 channel with the existing E99-114 data-set is the topic of a PhD thesis at the University of Glasgow and is currently at an advanced stage. These pion photoproduction results will prove very important in confirming the absence of precocious scaling already observed in WACS and lead to a fuller understanding of wide-angle reactions with high-energy electromagnetic probes.

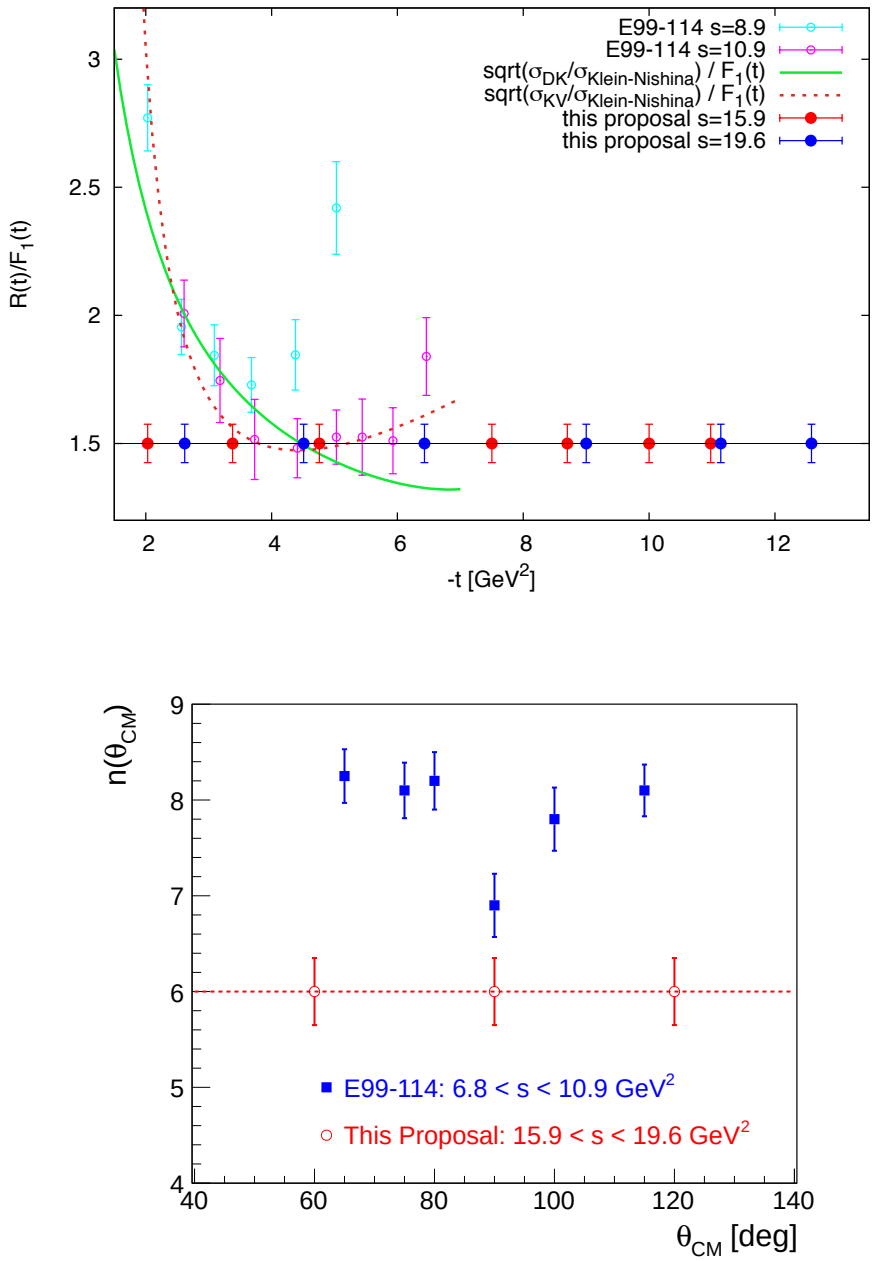

Figure 14: Expected precision achievable with the proposed measurements on the Compton form factor $\mathcal{R}$ (top) and scaling parameter n (bottom). The values for the cross section used for both plots were taken from an extrapolation of E99-114 data. The scaling parameter n was calculated for only three points in θ_{cm} for the purposes of this plot; its determination over a wider range of angles will be possible.

6 Technical Considerations

A key new element of instrumentation in this experiment is the photon calorimeter, the Neutral Particle Spectrometer, which is proposed for construction in Hall C by the NPS collaboration [37]. An additional element is a deflection magnet as discussed in Sec. 3 and below.

6.1 The Deflection Magnet

Our MC analysis (see Sec. 4) shows that for the WACS experiment the horizontal direction of the field is a significantly better choice because there is a higher resolution for the out-of-plane correlation between the proton and electron momenta than for the in-plane correlation. At large scattering angles, when the required solid angle of the photon arm is very large, the calorimeter will be placed very close to the target (2.5 m), which results in a significant 0.6 Tm field integral in the magnet. Due to the considerations above, we propose to construct a deflection magnet as shown in Fig. 15. It will have a weight of 9.5 tons and require 150 kW power. Because of the significant width of the magnet (a total of 100 cm with a 32 cm gap), a 16-cm tall cut in the left side yoke is made for the beam line path. Such a cut allows sufficient space for the magnetic shielding of the beam line. The residual transverse field integral on the beam line is of 100 Gauss-meter. It will require an additional small dipole corrector to nullify the total field integral on the beam line.

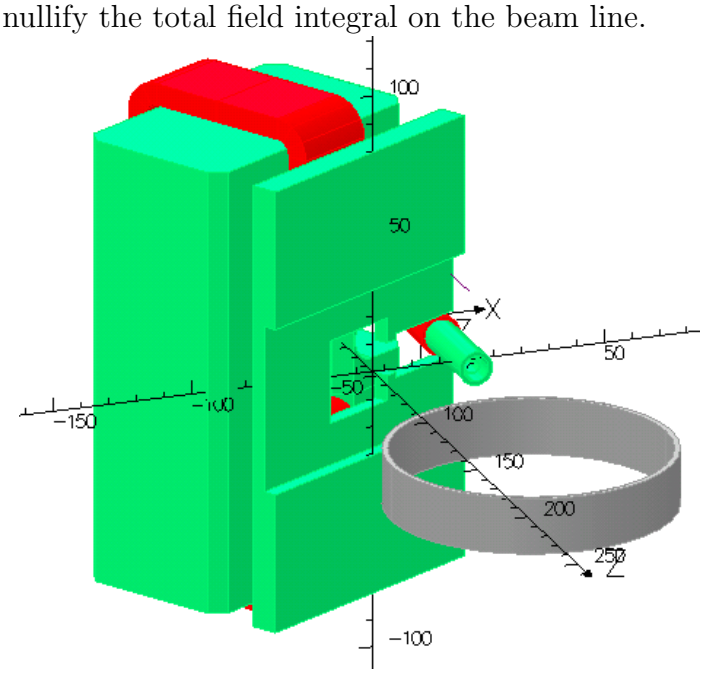

Figure 15: A picture of the deflection magnet for the WACS experiment from the TOSCA analysis package. In this picture the magnet is placed at a 30 degree scattering angle with 110 cm between the magnet center and the target.

6.2 Projected Radiation Budget for the NPS and the Radiation Level in Hall C

The average energy flow in the calorimeter for the 5F kinematic conditions will lead to a radiation dose rate in the calorimeter of 0.18 krad per hour according to the MC based calculation [37]. The radiation budget for the calorimeter over the full experiment was estimated at 150 krad, which is significant but still acceptable according to a study [41], which found that at a value of 1 Mrad, the light output reduction is about 2%. It is useful to note that interpolation of the empirical data of the E99-114 run to the conditions of this proposal leads to a lower radiation budget of 60 krad.

Using the data from the E99-114 run (Fig. 16), we also found an estimate for the radiation level in Hall C during the proposed experiment, which is of the order of 200 mR/hour. The radiation could be reduced by a factor of 2, if necessary, by using modest local shielding of the radiator and the target installed at angles above 50°.

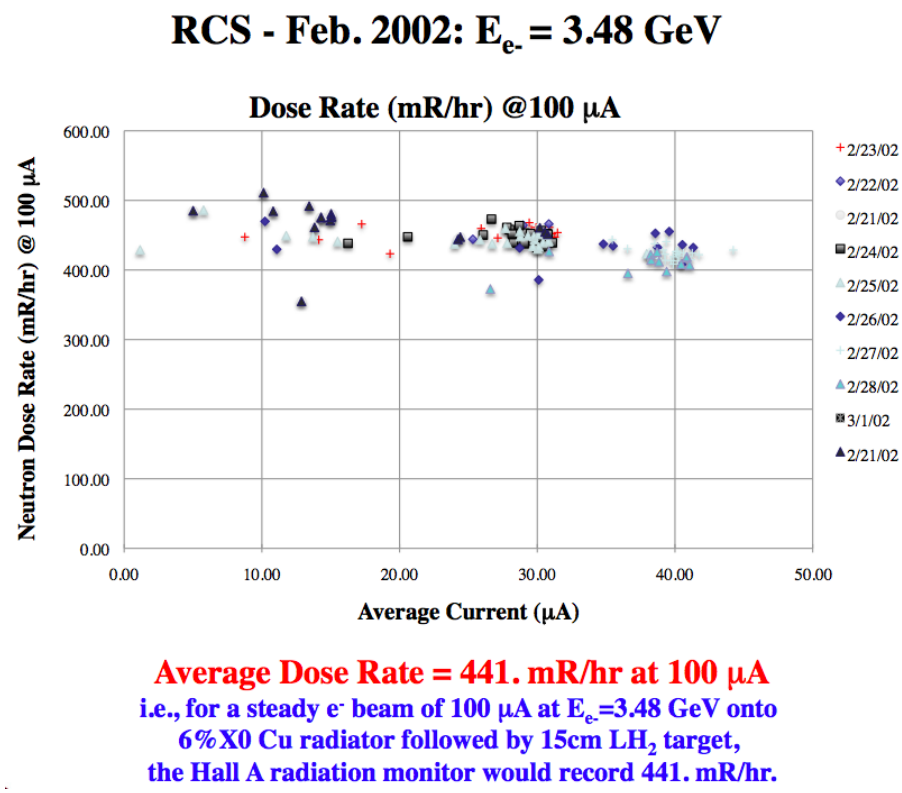

Figure 16: Radiation dose rate in Hall A during the E99-114 run from Ref. [42].

7 Conclusions

We request 1000 hours of beam-time to measure the cross section for proton Compton scattering in the wide-angle regime with 10% accuracy (combined statistical and systematic) at s= 15.9 and 19.6 (GeV/c)^2 at 13 kinematic points. This experiment will take place in Hall C, utilizing the HMS spectrometer to detect recoil protons, and the Neutral Particle Spectrometer to detect scattered photons. The experimental technique including the analysis procedure is tried and tested, the detector systems will be operating well within their capabilities, and the radiation levels on the calorimeter and in the hall are manageable. The beam-time request implicitly includes overheads for dead-time, inefficiencies, configuration changes and calibration runs.

Knowledge of the cross section for WACS at these kinematics will allow for a rigorous test of the validity of factorization for exclusive photo-induced reactions at high s and t. It will establish the scaling behavior of the cross section in this new kinematic regime, helping with the understanding of the reaction mechanism for Compton scattering, and provide crucial insights into the fundamental nature of nucleon structure in the high-t valence region. In addition, the data will help in the understanding of the two-photon exchange mechanism in elastic ep scattering, and will be used for a high-precision measurement of the neutral pion photoproduction cross section.

References

[1] N. Kivel and M. Vanderhaeghen, *JHEP* 1304 (2013) 029; arXiv:1212.0683.

[2] A.V. Radyushkin, *Phys. Rev.* **D 58**, 114008 (1998).

[3] M. Diehl, T. Feldmann, R. Jakob, P. Kroll, *Eur. Phys. J.* **C 8**, 409 (1999).

[4] H. W. Huang, P. Kroll, T. Morii, *Eur. Phys. J.* **C 23**, 301 (2002).

[5] M. Diehl and P. Kroll, arXiv:1302.4604.

[6] G. Eichmann and C. S. Fischer, *Phys. Rev.* **D 87** , 036006 (2013); arXiv:1212.1761.

[7] C. D. Roberts, *Prog. Part. Nucl. Phys.* 61, 50 (2008); I. C. Cloët, G. Eichmann, B. El-Bennich, T. Klahn, and C. D. Roberts, *Few Body Syst.* 46, 1 (2009).

[8] I. C. Cloë, C. D. Roberts, A. W. Thomas, arXiv:1304.0855.

[9] G. R. Farrar and H. Zhang, *Phys. Rev. Lett.* **41**, (1990) 1721, *Phys. Rev.* **D 65** (1990) 3348.

[10] A. S. Kronfeld and B. Nizic, *Phys. Rev.* **D 44**, 3445 (1991).

[11] M. Vanderhaeghen, P. A. M. Guichon and J. Van de Wiele, *Nucl. Phys.* **A 622**, 144c (1997).

[12] T. Brooks and L. Dixon, *Phys. Rev.* **D 62** 114021 (2000).

[13] R. Thomson, Alex Pang, and Cheng-Ryong Ji, *Phys. Rev.* **D 73** 054023 (2006).

[14] C. Hyde-Wright, A. Nathan, and B. Wojtsekhowski, spokespersons, JLab experiment E99-114.

[15] A. Danagoulian, V. H. Mamyan *et al.*, *Phys. Rev. Lett.* **98**, 152001 (2007).

[16] M. A. Shupe *et al.*, *Phys. Rev.* **D 19**, 1921 (1979).

[17] D. J. Hamilton, V. H. Mamyan *et al.*, *Phys. Rev. Lett.* **94**, 242001 (2005).

[18] M. Diehl *et al.*, *Phys. Rev.* **D 67**, 037502 (2003).

[19] G. A. Miller, *Phys. Rev.* **C 69**, 052201(R) (2004).

[20] F. Cano and J. M. Laget, *Phys. Lett.* **B 551**, 317 (2003).

[21] S. J. Brodsky and G. P. Lepage in *Perturbative Quantum Chromodynamics*, edited by A. Mueller (World Scientific, Singapore, 1989).

[22] S. J. Brodsky and G. Farrar, *Phys. Rev. Lett.* **31**, 1953 (1973).

[23] V. Matveev *et al.*, *Nuovo Cimento Lett.* **7**, 719 (1973).

[24] S. J. Brodsky and G. P. Lepage, *Phys. Rev.* **D 22**, 2157 (1980).

[25] M. Jones *et al.*, *Phys. Rev. Lett.* **84**, 1398 (2000).

[26] O. Gayou *et al.*, *Phys. Rev. Lett.* **88**, 092301 (2002).

[27] I. Pomerantz *et al.*, arXiv:1303.5049.

[28] F. Cano and J. M. Laget, Phys. Rev. D **65** (2002) 074022.

[29] X. Ji, *Phys. Rev.* **D 55**, 7114 (1997), *Phys. Rev. Lett.* **78**, 610 (1997).

[30] A.V. Radyushkin, *Phys. Lett.* **B 380**, 417 (1996), *Phys. Rev.* **D 56**, 5524 (1997).

[31] G. A. Miller and M. R. Frank, *Phys. Rev.* **C 65**, 065205 (2002)

[32] G. A. Miller, *Phys. Rev.* **C 66**, 032201 (2002)

[33] C. D. Roberts and A. G. Williams, Prog. Part. Nucl. Phys. **33**, 477 (1994).

[34] R. Gilman, A. Nathan, and B. Wojtsekhowski, spokespersons, JLab experiment E07-002.

[35] M. A. P. Carmignotto, *Neutral Particle Detector: Simulations*, Hall C Users Meeting, JLab, January 24, 2013.

[36] D. J. Hamilton *et al.*, Nucl. Instr. Meth. A **643** (2011) 17. See also PhD thesis (in progress) of C. Fanelli (INFN-ISS).

[37] R. Ent, T. Horn, H. Mkrtchyan, *et al.*(NPS Working Group), *Neutral-Pion Spectrometer Facility in Hall C*, Proposal to Jefferson Lab PAC40.

[38] M. Kubantsev et al., *Performance of the Primex Electromagnetic Calorimeter*, `arXiv:physics/0609201`, September 22, 2006; A. Gasparyan, *Performance of PWO crystal Detector for a High Resolution Hybrid Electromagnetic Calorimeter at Jefferson Lab*, Proceed. X Int. Conf. on Calorimetry in Particle Physics, Perugia, Italy, 29 March-2 April 2004, pp. 109-115.

[39] David J. Hamilton, *A simulation of the* 12 GeV *Hall C RCS experiment*, University of Glasgow, April 14, 2013 (unpublished).

[40] P.E. Bosted, Phys. Rev. C **51** (1995) 409.

[41] Ren-yuan Zhu, *Nucl. Instr. Meth.* **A 613** (1998) 297.

[42] J. Boyce, private communication.